Morphology of Deposits Formed from Chemically Heterogeneous Suspensions: Application to Membrane Filtration

Volodymyr V. Tarabara,* Françoise Pierrisnard,† Claude Parron,† Jean-Yves Bottero,† and Mark R. Wiesner*,[1]

*Environmental and Energy Systems Institute, Rice University, Houston, Texas 77006-1892; and †Université Aix-Marseille III-CNRS, C.E.R.E.G.E. (Centre Européen de Recherche et d'Enseignement de Géosciences de l'Environnement), Unité Mixte de Recherche 6635, Europôle Méditerranéen de l'Arbois, B.P. 80, 13545 Aix-en-Provence cedex 04, France

The morphology of fouling layers is an important factor in modeling permeate flux behavior in membrane filtration. In the present paper, the relationship between the chemical composition of suspension and the morphological properties of the deposit formed from the suspension was studied. The deposition from binary suspensions of particles with different collision efficiencies as a prototype for naturally occurring heterogeneous suspensions was simulated using the 2D on-lattice deposition model. Simulation results were qualitatively compared with transmission electron microscopy and energy-dispersive X-ray analysis of fouling layers produced in a series of pilot filtration experiments. For the case of deposition from binary suspensions, different degrees of segregation of chemically distinct particulate fractions in the fouling layer were observed. Similar deposition patterns were observed in the pilot filtration experiments; the fouling layers consisted of an organic matrix with dendritic inclusions of metallic nature. These findings prompt reevaluation of the model of resistances connected in series for the fouling layer resistance usually employed to describe permeate flow. Chemical heterogeneity of suspension may result in the formation of fouling layers with substructures of different specific resistances to permeate flow. The total resistance can be expected to be less than predicted in the assumption of a chemically homogeneous suspension. © 2002 Elsevier Science (USA)

Key Words: particle deposition; collision efficiency; membrane filtration; fouling layer morphology; fractal dimension.

INTRODUCTION

Emergence of membrane filtration as one of the most reliable and cost-effective unit processes for water treatment has stimulated much research on the fundamental physical chemical processes underlying membrane operation (1–5). Particle deposition and fouling have been recognized as a problem to be controlled in membrane system operation and design. Models accounting for different particle transport mechanisms have been proposed (6–9). However, comparison of the experimental and modeling results reveals deficiencies in the description of

transient and steady state permeate flux in membrane filtration operation (3, 10).

One reason proposed to account for discrepancies between predicted and observed fluxes is the inadequate treatment of properties of the fouling layer formed at the membrane surface in the course of filtration (11, 12). The morphology of a fouling layer determines the resistance imparted by the layer to permeate flow (2) as well as the fouling layer's reversibility (13). Thus, predicting morphology of fouling layer as a function of operational parameters such as transmembrane pressure, crossflow velocity, surface chemistry of fouling particles, etc., is a key step toward description of the permeate flux behavior. This assertion has been corroborated by several recently published studies of the coupling between permeate flux and fouling layer properties (14–17).

One possible approach to studying fouling layer formation is consideration of this process as consisting of two consecutive steps (11, 18–20): (a) long-range transport of particles to the surface followed by (b) (multiple) attachment event(s) that may be considered as short-range phenomena greatly influenced by particle surface chemistry. This approach allows, to a certain extent, for a separate consideration of the physical and chemical processes involved.

Transport of particles to the deposit is governed by the interplay of diffusive (Brownian diffusion, turbulent diffusion, shear-induced diffusion) and convective transport processes (crossflow and permeate fluxes) as well as transport processes due to external forces (e.g., electrostatic attraction, centrifugal force) (12). The relative importance of ballistic (deterministic) and diffusive (stochastic) particle transport in the system may be characterized by a particle Peclet number $Pe = \frac{vL}{D_{tot}}$, where v is particle velocity, L is particle diameter, and D_{tot} encompasses particle diffusivity by all mechanisms. Deposits formed from ballistically transported (high Pe) particles are known to be denser than deposits formed from diffusively transported (low Pe) particles (21).

The attachment step can be described by the particles' collision efficiency α (or sticking probability) (22). The more cohesive the particles, the higher their collision efficiency; with $\alpha = 1$ for perfectly cohesive particles. The factors determining the potential for interaction between particles, and, as a consequence,

the value of α, are the chemistry of the aqueous phase and surface chemical properties of the particles.

In this paper we present results of 2D Monte Carlo on-lattice modeling of particle deposition onto permeable substrate. First, the deposition from suspension of particles of one type was simulated. Effects of different long-range and short-range transport regimes, modeled by changing Pe and α correspondingly, on the morphology of deposits were studied and quantitatively compared. Second, the deposition from binary suspensions of particles with different collision efficiencies as a prototype for naturally occurring heterogeneous suspensions was modeled. Finally, simulation results were compared with deposits formed during membrane filtration. The morphology and chemical composition of fouling layers formed in the course of a pilot filtration study, performed at the nanofiltration facility in Mary-sur-Oise (France) (23), were imaged by transmission electron microscopy (TEM) and characterized by energy-dispersive X-ray analysis (EDX).

METHODS

Deposition Modeling

Deposition algorithm.   The simulation of deposition from a monodisperse suspension of spherical particles was performed using a modified version of a generic 2D on-lattice algorithm described elsewhere (24). In the generic model, particles were introduced into the simulation domain one by one at a release line above the deposit at a random horizontal position along the substrate. A released particle underwent a random walk biased according to the force balance on the particle. A pseudo-Peclet number was used to determine the distribution of probability of movement in one of eight directions on the 2D grid for the particle,

$$N_{Pe} = \frac{V_g + V_{pf}}{V_d} \qquad [1]$$

where V_g, V_{pf}, and V_d are particle velocities due to gravity, permeate flow, and diffusion, correspondingly. The lattice was 1000×1000 with periodical boundary conditions imposed on its side boundaries. To model the propensity of particles in suspension to attach to the deposit upon contact, another parameter, collision efficiency α, was used. Collision efficiency was defined as the probability that collision results in adhesion of the particle to the deposit. A collision that did not result in attachment was followed by further migration of the particle in a direction determined by the local structure of the deposit and a force balance on the particle. Attachment occurred only at the sites of nearest neighbors of occupied sites.

The generic algorithm was modified to model the chemical heterogeneity of a depositing suspension. The simple case of a binary suspension consisting of two sorts of particles, each sort having its own surface chemistry, was modeled. Particles were assigned "colors" (gray and black) and corresponding collision efficiencies α_{ij}. For the case of a binary suspension, three values of collision efficiency—α_{gg}, α_{bb}, and α_{gb}—were needed to characterize collisions between gray particles, between black particles, and between two particles of different color, correspondingly. A particle's color was determined by generating a random number in the [0, 1] range and comparing it with a predefined number F, which represents the fraction of particles of a given type present in the suspension.

Quantitative characterization of deposits.   Deposits were quantitatively characterized in terms of their fractal dimension (25). In the course of generating each deposit, its fractal dimension D was calculated from the $\bar{h} \propto N^{\frac{1}{D-1}}$ relationship, where $\bar{h}$ is the average height of the deposit and N is the number of deposited particles corresponding to $\bar{h}$ in the growing deposit (26). However, a single value of fractal dimension is insufficient to characterize deposits completely, as deposits with visually different morphologies may yield the same fractal dimension. Further characterization of the deposit included a determination of the growth site probability distribution (GSPD).

For each deposit, the GSPD was calculated using the technique of probe particles (26). This method is based on the same deposition algorithm used to form a deposit. However, instead of releasing new particles, probe particles (probes) were released at the top of the lattice containing the deposit. Probe particles are distinguished by the property that a probe disappears at the moment when "regular" particles would attach to the deposit. While regular particles modify the deposit by attaching to it, probes explore the deposit by touching it. Probes are transported in the same manner as regular particles and their surface chemistry is characterized by a collision efficiency α_{probe}. By changing α_{probe}, it is possible to vary the ability of a probe to enter sinuous "fjords" in the deposit. At each location on the deposit, the number of times a site is touched by a probe under conditions corresponding to an attachment event of a regular particle was counted. After a certain number of probes were released, the counts for each site on the deposit were read and plotted. The higher the number of probes released, and the lower the collision efficiency α_{probe}, the higher the number of sites that should have non-zero readings and, hence, more detailed information about the surface can be gathered. In the present work, 50,000 probes having the same collision efficiency of 10^{-4} were released. For each location at the deposit surface the number of contacts by a probe was calculated and divided by 50,000 so that the normalized GSPD was obtained.

Once known, the GSPD may be used to obtain information about the surface properties of deposits. This information allows one to discriminate between deposits of the same D but formed under different conditions (e.g., one deposit formed at higher N_{Pe} and another one formed at lower α). Loci of sites contacted by probes at least once may be considered to represent the deposit's surface. In the case of the deposition from heterogeneous suspensions, a color may be assigned to each chemically distinct suspension fraction, and the color of particles located at the deposit's surface will then determine the surface chemistry of the deposit.
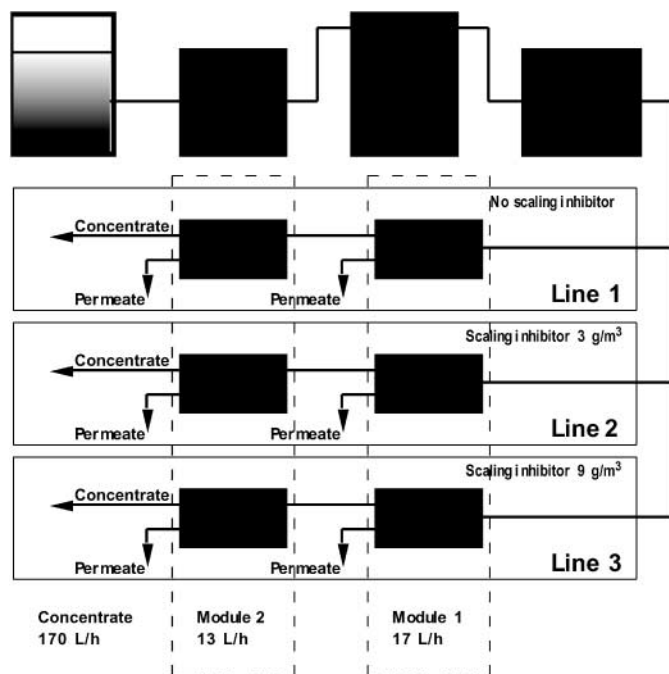
FIG. 1. Flow chart of the nanofiltration pilot.

Crossflow Nanofiltration Pilot Study

A crossflow nanofiltration pilot experiment 1683 h long was carried out at the Mary-sur-Oise water treatment plant (France) (23). Chemical and morphological characterizations of fouling layers formed at the membrane surface for different doses of scaling inhibitor added to the feed flow were performed.

Filtration experiments. The configuration of the pilot is shown in Fig. 1. The pilot comprised six spiral wound membrane modules each measuring 6.25 cm in diameter and 100 cm in the direction of flow. Each module consisted of two spacer-separated membranes rolled around a spherical collector. Membranes were FILMTEC NF 200B (Dow Chemical Co.) with a filtering surface of 2.1 m^2 and a molecular weight cutoff of 200 Da. A constant feed flow of 600 L/h was distributed to three parallel treatment trains (Line 1, Line 2, and Line 3). Each line consisted of two membrane modules connected in series (Module 1 and Module 2 in the direction of flow). Permeate flow was collected from Module 1 at the rate of 17 L/h in each line and from Module 2 at the rate of 13 L/h in each line; 170 L/h of concentrate flow was collected at the exit of each line. At the entrance to Line 2 and Line 3 a scaling inhibitor (mixture of phosphoric acid and polycarboxylate) was added at concentrations of 3 and 9 g/m^3, respectively. No scaling inhibitor was added to Line 1 which served as a control. After filtration, all membranes from Module 2 were subjected to acid–base cleaning while membranes from Module 1 were not cleaned. Fouled membranes were transported from the plant to the CEREGE laboratory in isothermal vessels and were stored at 8°C to prevent bacterial proliferation.

Morphological and local chemical characterization of fouling layers. The membranes were unrolled and square fragments with areas of several square micrometers were cut out from the membrane. These fragments were dried in the oven at 40°C. A solution composed of glutaraldehyde, sacharose, and sodium phosphate buffer was used to chemically fix the fragments. Subsequently, the fragments were treated with osmium tetroxide as a postfixation agent and dehydrated. Finally the samples were embedded in a resin (ether glycidical) matrix that was polymerized for 3 h at 60°C. An ultramicrotome was used to cut the prepared fragments of the fouling layer into slices thin enough, 500–700 Å, for TEM imaging. The slices were put onto the microscope's copper grid and covered with a thin carbon layer. A transmission electron microscope JEOL 2010 (Centre Pluridisciplinaire de Microscopie et Microanalyses de la Faculté de Saint-Jérôme, Université d'Aix-Marseille III) was operated at 200 kV. TEM image resolution provided by the JEOL 2010 was 2 Å. Apart from producing TEM images of the samples, the JEOL 2010 was also used for local elemental analyses of fouling layers by EDX. The samples were probed with a 0.5- to 1-nm-diameter electron beam.

Integral characterization of chemical composition of fouling layers. Bigger fragments with areas of several square centimeters were also cut from the membranes. These fragments were submerged in ultrapure water and ultrasonicated to separate fouling layers from the membranes. The separated layers were lyophilized and weighed to estimate the mass of foulant per unit area of a membrane. Atomic absorption spectra and infrared spectra of the lyophilized fouling layers were then recorded to characterize their chemical composition.

RESULTS

Simulation Results

Morphology of deposits formed in different long- and short-range transport regimes. One of the goals of this work was to study and compare the effects of two parameters, α and N_{Pe}, characterizing short- and long-range transport of particles to the deposit correspondingly, on the morphology of the deposit. In doing this, deposits formed from perfectly cohesive particles ($\alpha = 1$) transported at four different values of N_{Pe} were generated (Fig. 2). Operational parameters are indicated in Table 1 (sims. 1–4). Further, to simulate the effect of collision efficiency, the model was also run for the case of particles having the same $N_{Pe} = 7.6 \times 10^{-2}$ value but different values of α (Fig. 3, sims. 5–8).

To compute fractal dimensions, the model was run several times for each combination of α and N_{Pe}. Specifically, three runs were done for all combinations of α and N_{Pe} where $N_{Pe} > 1.06 \times 10^{-2}$ and six runs were done for all combinations of α and N_{Pe} where $N_{Pe} < 1.06 \times 10^{-2}$. More runs for the latter case were performed because of the higher scatter in statistics collected at low N_{Pe} values. The higher scatter for calculated D values was due to the smaller number of particles in more open
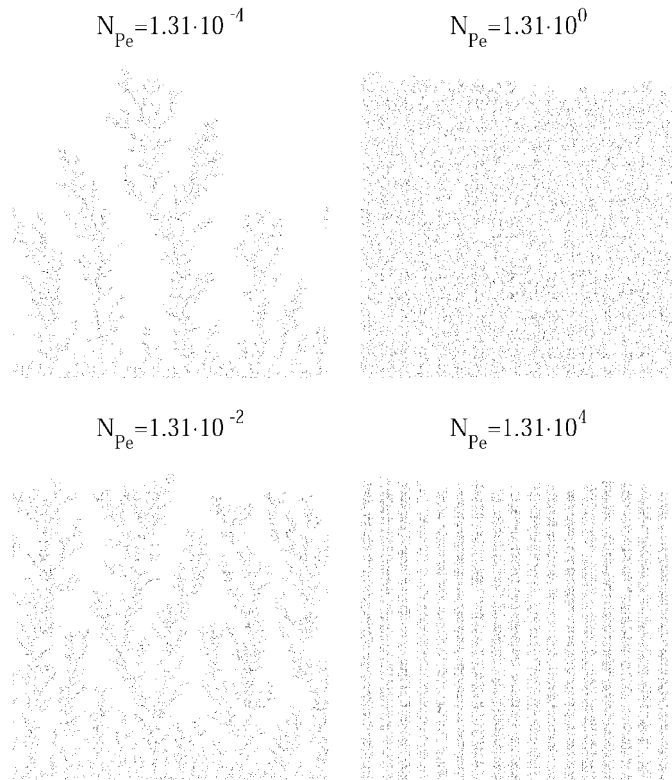
FIG. 2. Simulated deposit formed from perfectly cohesive particles ($\alpha = 1$) at different values of N_{Pe}: 1.31×10^{-4}, 1.31×10^{-2}, 1.31×10^{0}, and $1.31 \times 10^{+4}$.
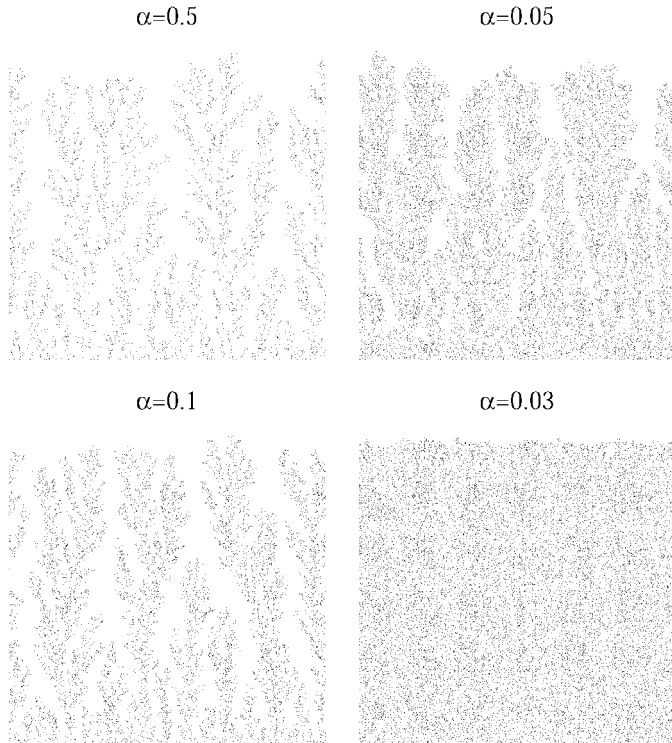

FIG. 3. Simulated deposit formed from particles with different collision efficiencies: $\alpha = 0.50, 0.10, 0.05$, and 0.03.
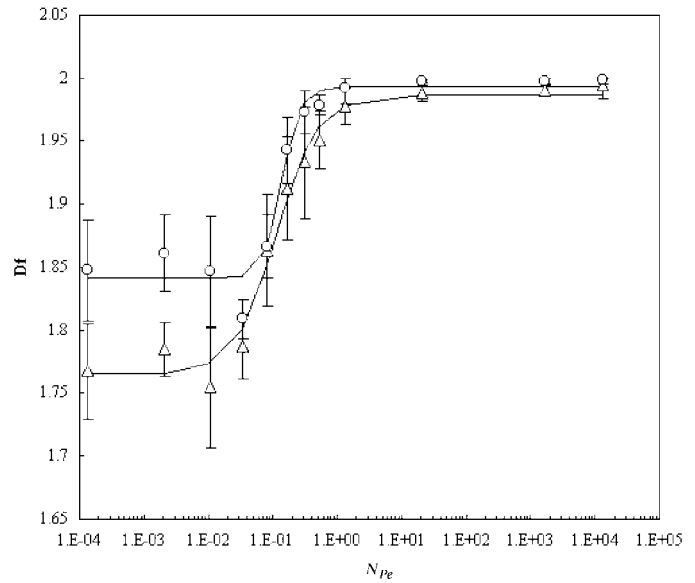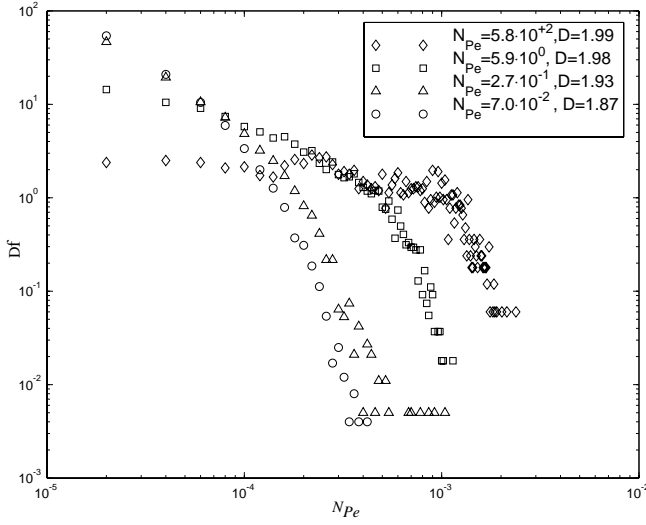

FIG. 4. Fractal dimension of deposit as a function of Peclet number for two different collision efficiencies: $\alpha = 0.1$ (symbols $\bigcirc$) and $\alpha = 1$ (symbols $\triangle$).

deposits formed at low N_{Pe}. The corresponding values of D were obtained by averaging the results of the corresponding number of runs. The dependence of D on α for different N_{Pe} values is summarized in Fig. 4. Error bars correspond to a 90% confidence interval. As expected, an increase in N_{Pe} and a decrease in α lead to formation of deposits with higher fractal dimensions. It was observed that at large values of N_{Pe}, compact deposits were formed and $D \rightarrow 2$ for all values of α. In the case of small N_{Pe} values, though, substantial differences in the morphology were observed. For $\alpha = 1$, for example, D converged to 1.77 (1.7 being the theoretical value for diffusion-limited growth), while for $\alpha = 0.1$ D was higher and converged to 1.84.

GSPD analysis. From a comparison of Figs. 2 and 3, it is evident that changes in deposit morphology induced by changes in α differ from those induced by changes in N_{Pe}. In the former case, a decrease in α results in a thickening of the branches of the deposits. This is in sharp contrast with the latter case, where an increasingly ballistic character of deposition leads to formation of an increasingly dense web-like structure, more homogeneously distributed in space.

Despite the very apparent differences between these structures, the two deposits may be characterized by the same fractal dimension. Consider the case where D increases from 1.7 to a higher value due to an increase in N_{Pe}, while a similar increase in D is produced due to a decrease in α. To distinguish between two such deposits of equal fractal dimension and characterize the deposits more completely, the GSPD was computed for each deposit. Normalized GSPDs for all eight deposits are represented in Figs. 5 and 6. In these figures:

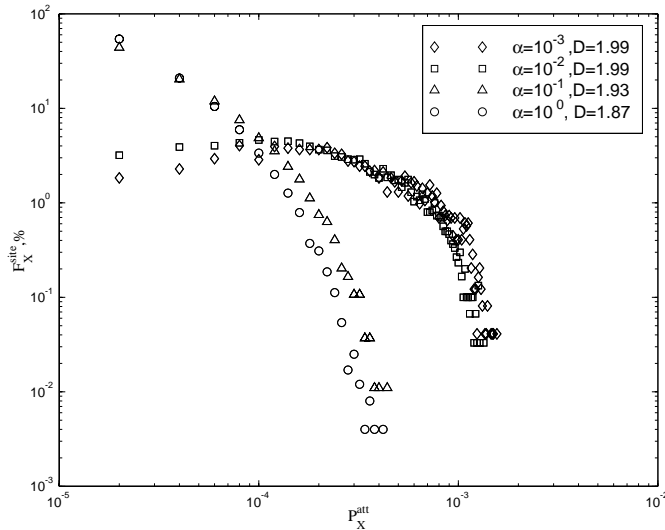$$P_X^{att} = \frac{N_X^{att}}{N_{total}^{att}}$$ [2]

FIG. 5. GSPDs for deposits formed at different N_{Pe}.

$$F_X^{\text{site}} = \frac{N_X^{\text{site}}}{N_{\text{total}}^{\text{att.site}}} \cdot 100\%, \qquad [3]$$
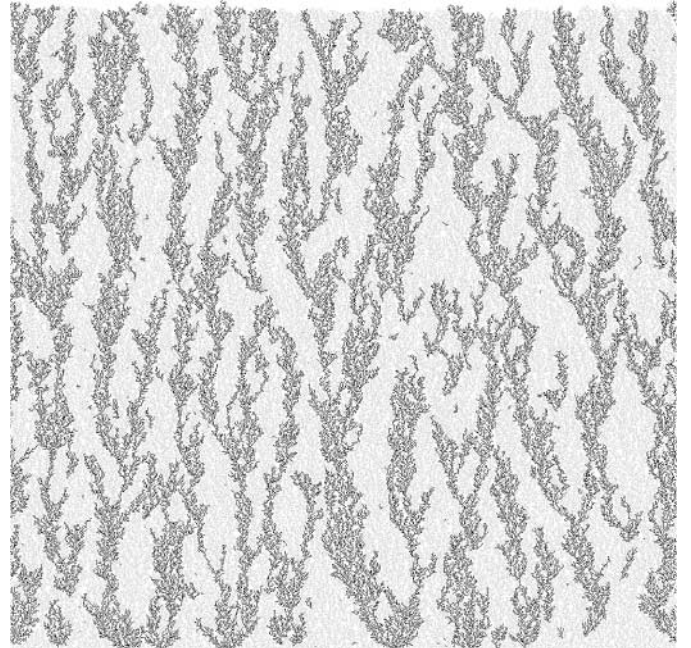
where

P_X^{att} is the probability of attachment at a site X,

N_X^{att} the number of attachments at a site X,

$N_{\text{total}}^{\text{att}}$ the total number of attachments,

F_X^{site} the percentage of sites X,

N_X^{site} the number of sites X, and

$N_{\text{total}}^{\text{att.site}}$ the total number of attachment sites.

Deposition from binary suspensions. Deposits formed from binary suspensions with different combinations of the parameters involved were modeled. Simulation parameters are summa-

TABLE 1
Simulation Parameters

Simulation no.	α_{gg}	α_{bg}	α_{bb}	N_{Pe}	F_{gray}
1	10^0	10^0	10^0	1.31×10^{-4}	1
2	10^0	10^0	10^0	1.31×10^{-2}	1
3	10^0	10^0	10^0	1.31×10^0	1
4	10^0	10^0	10^0	1.31×10^4	1
5	5.0×10^{-1}	5.0×10^{-1}	5.0×10^{-1}	7.6×10^{-2}	1
6	1.0×10^{-1}	1.0×10^{-1}	1.0×10^{-1}	7.6×10^{-2}	1
7	5.0×10^{-2}	5.0×10^{-2}	5.0×10^{-2}	7.6×10^{-2}	1
8	3.0×10^{-2}	3.0×10^{-2}	3.0×10^{-2}	7.6×10^{-2}	1
9	10^{-3}	10^{-5}	10^{-2}	7.6×10^{-2}	0.5
10	10^{-3}	10^{-4}	10^{-2}	7.6×10^{-2}	0.5
11	10^{-3}	10^{-6}	10^{-2}	7.6×10^{-2}	0.5
12	10^{-3}	10^{-5}	10^{-2}	7.6×10^{-2}	0.7
13	10^{-3}	10^{-5}	10^{-2}	7.6×10^{-2}	0.9
14	10^{-3}	10^{-5}	10^{-2}	1.2×10^{-4}	0.5
15	10^{-2}	10^{-3}	10^{-1}	7.6×10^{-2}	0.5
16	10^{-2}	10^{-3}	10^{-1}	1.2×10^{-4}	0.5
17	10^{-3}	10^{-5}	10^{-2}	1.2×10^{-4}	0.9
18	10^{-3}	10^{-5}	10^{-2}	1.2×10^{-4}	0.7
19	10^{-2}	10^{-2}	10^{-1}	1.2×10^{-4}	0.5
20	10^{-2}	10^{-1}	10^{-2}	1.2×10^{-4}	0.5
21	10^{-1}	10^{-3}	10^{-1}	1.2×10^{-4}	0.5

rized in Table 1 (sims. 9–21). Effects of α_{bg} (sims. 16 and 19; sims. 9–11; Figs. 7 and 8), N_{Pe} (sims. 9 and 14; sims. 15 and 16), and fraction F of particles of one type (sims. 9, 12, and 13; Figs. 7 and 9) were studied. The case $\alpha_{\text{bg}} \geq, \alpha_{\text{bb}}, \alpha_{\text{gg}}$ (sim. 20) is

FIG. 6. GSPDs for deposits formed at different α.

FIG. 7. Deposit formed from binary suspension of particles with collision efficiencies $\alpha_{\text{gg}} = 10^{-3}$, $\alpha_{\text{bg}} = 10^{-5}$, and $\alpha_{\text{bb}} = 10^{-2}$, and $N_{Pe} = 7.6 \times 10^{-2}$. Fraction of gray particles, $F = 0.5$.

FIG. 8. Deposit formed from binary suspension of particles with collision efficiencies $\alpha_{gg} = 10^{-3}$, $\alpha_{bg} = 10^{-4}$, $\alpha_{bb} = 10^{-2}$, and $N_{Pe} = 7.6 \times 10^{-2}$. Fraction of gray particles, $F = 0.5$.
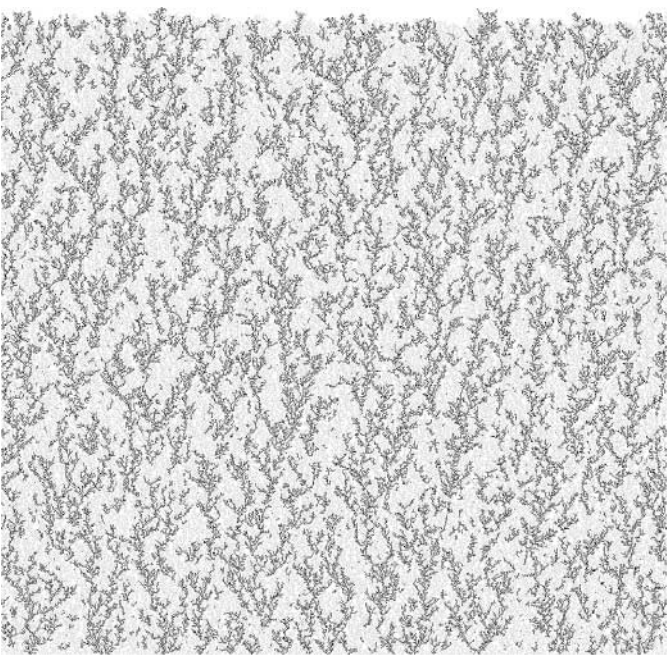
trivial—gray particles attach to black ones and vice versa and the chessboard-like pattern results (not shown). Thus, the nontrivial case $\alpha_{bg} \leq \alpha_{bb}, \alpha_{gg}$ is of more interest. First, the case $\alpha_{bb} \neq \alpha_{gg}$ was studied. The probability of sticking between black particles
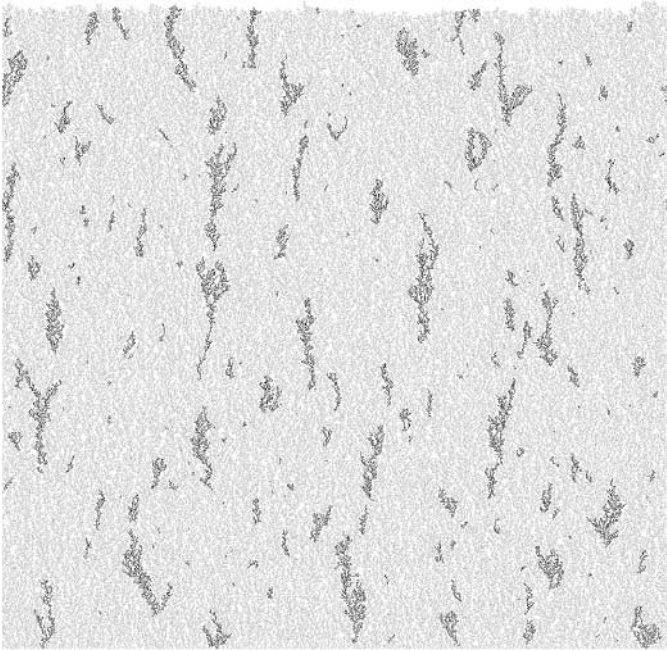

FIG. 9. Deposit formed from binary suspension of particles with collision efficiencies $\alpha_{gg} = 10^{-3}$, $\alpha_{bg} = 10^{-5}$, $\alpha_{bb} = 10^{-2}$, and $N_{Pe} = 7.6 \times 10^{-2}$. Fraction of gray particles, $F = 0.9$.

(α_{bb}) was taken to be bigger than that between gray ones (α_{gg}): $\alpha_{bb} \geq \alpha_{gg}$. Deposits formed at higher values of N_{Pe} were denser, characterized by higher values of D, as expected. Absolute values of collision efficiencies were found to have a major impact on the relative distribution of particles of different types in the deposit. First, a decrease in α_{bg} led to an increase in the segregation of particles of different types (sims. 9–11; sims. 16 and 19; Figs. 7 and 8). Second, the structure of deposits was determined primarily by particles with the larger values of α (cohesive fraction), while particles with the smaller values of α (noncohesive fraction) dominated the surface of deposits. Depositing cohesive particles formed a network-like structure that was filled by particles from the noncohesive fraction. It should be noted that this structure became discontinuous when the fraction of noncohesive particles was increased to 0.9 (sims. 9, 12, and 13; Figs. 7 and 9). The more strict the $\alpha_{bg} \leq \alpha_{bb}, \alpha_{gg}$ condition, the more pronounced the segregation of particles from different sets into substructures elongated in the direction normal to the membrane surface (sims. 9–11; Figs. 7 and 8). In turn, the elongation was more pronounced for the case of higher N_{Pe}, i.e., when the direction of bias in the particle's random walk was "more preferential." It should be noted that a decrease in the values of α_{gg} and α_{bb} with a fixed value of α_{bg} (sims. 14 and 16) resulted in a higher degree of segregation, but not in changes in the segregation pattern; particles from the less cohesive fraction filled the spaces between branching structures formed from more cohesive particles. In the other case, when $\alpha_{bb} = \alpha_{gg}$, an independent growth of gray and black structures was observed (sim. 21, not shown) with the deposition pattern being symmetrical with respect to particles of different types, as anticipated.

Surface characterization. For the deposit generated in simulation 5 (see Table 1), 50,000 probes were released for five cases of different values of probe's collision efficiency: $\alpha_{probe} = 10^0, 10^{-1}, 10^{-2}, 10^{-3}, 10^{-4}$, and 10^{-5}. Table 2 illustrates (a) the total amount of sites detected by the probes at the surface of the deposit, i.e., surface "length," and (b) the amount of gray particles at the surface characterizing the degree of surface segregation. With α_{probe} decreasing, more and more inner regions of the deposit appear accessible to the probes. Gray particles (less cohesive fraction) dominate the easily accessible regions of the deposits and become even more abundant on the surface of the hardest to reach parts of the deposit surface. This

TABLE 2
Surface Characterization of Simulated Deposits

Simulation no.	α_{probe}	Percentage of gray particles at surface	Length of surface
1	10^0	56.5 ± 3.2	2700 ± 287
2	10^{-1}	59.0 ± 3.2	3951 ± 205
3	10^{-2}	63.5 ± 3.2	6078 ± 1025
4	10^{-3}	68.5 ± 3.2	10830 ± 672
5	10^{-4}	70.5 ± 3.2	13631 ± 1476
6	10^{-5}	72	14776

Towards the top of the fouling layer

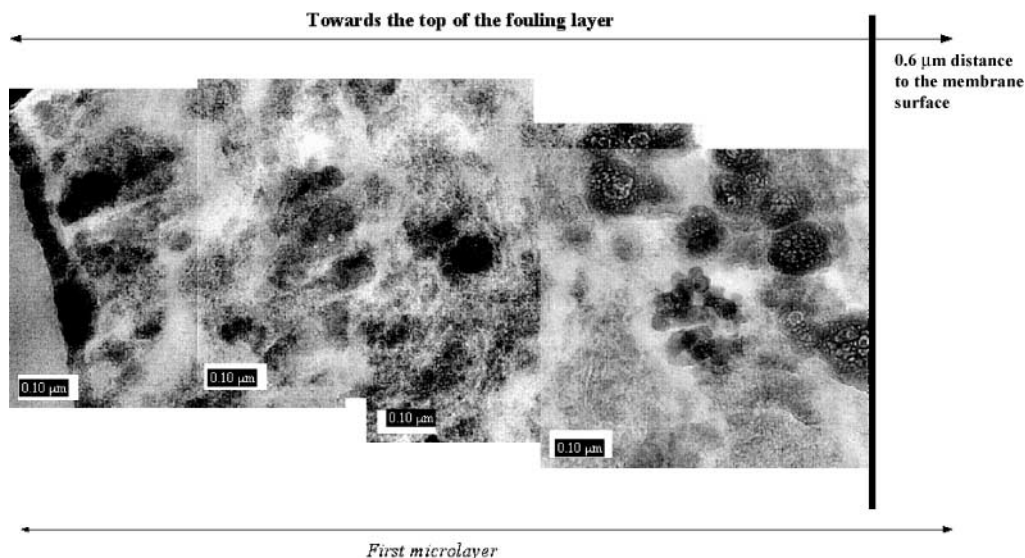0.6 μm distance to the membrane surface

First microlayer

FIG. 10. Fouling layer in Line 1. No scaling inhibitor added.

is an anticipated result—because it takes more collisions with the deposit for particles with smaller collision efficiency to attach permanently, these particles are more likely to penetrate the fjords without being attached to the fjords' walls at its entrance. This means that the particles from the less cohesive fraction are the last to attach and, hence, they determine the surface chemistry of the deposit.

Experimental Results

In this work, results of TEM and EDX studies of fouled (not cleaned) membranes are reported in an effort to explain foul-

ing layer morphologies observed by comparing them with results of the model presented above. Other details of the pilot study are presented elsewhere (27). Analysis of TEM images (Figs. 10–12) revealed that fouling layers had a zonal structure with strata varying in thickness, morphology, and chemical composition. Another salient feature of all fouling layers examined was that they could be characterized as an organic matrix incorporating mineral inclusions arranged in a fractal pattern. These similarities and differences in structure and composition of the fouling layers formed on the surfaces of membranes from each Line are described in detail in the following paragraphs and summarized in Fig. 13.
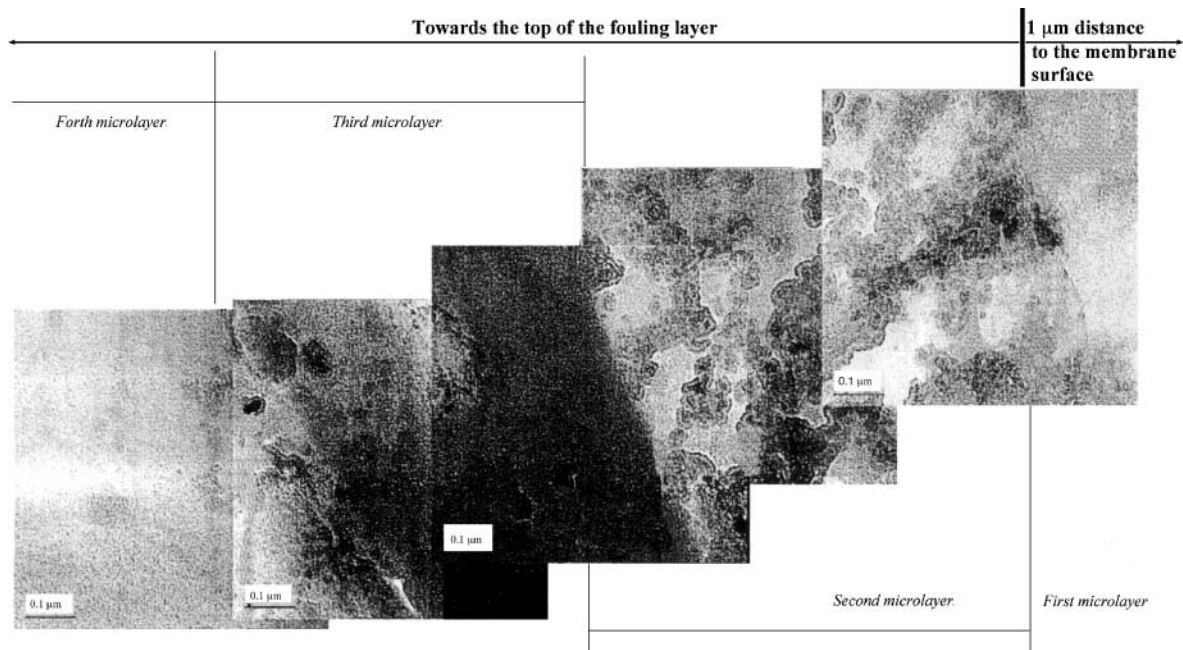

Towards the top of the fouling layer

1 μm distance to the membrane surface

Forth microlayer *Third microlayer*

Second microlayer *First microlayer*

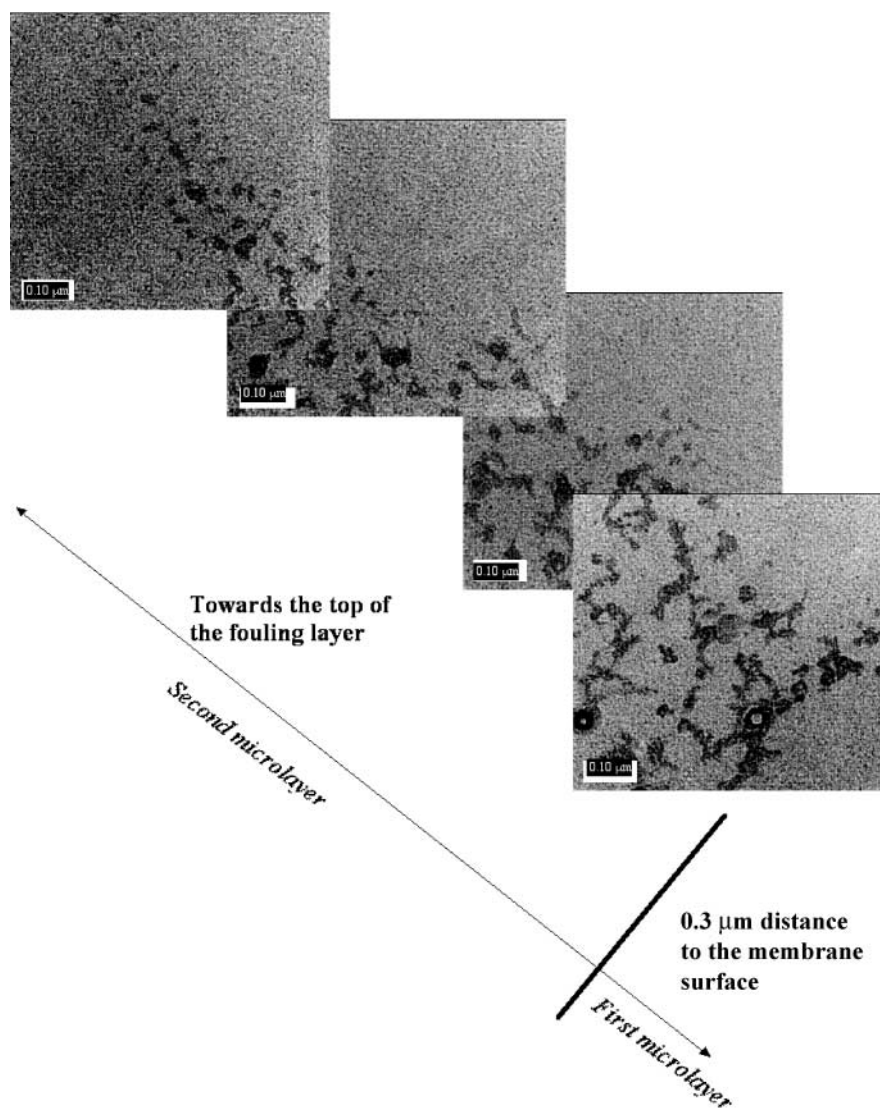**FIG. 11.** Fouling layer in Line 2. Scaling inhibitor dose, 3 g/m^3.

FIG. 12. Fouling Layer in Line 3. Scaling inhibitor dose, 9 g/m^3.

Line 1. As already mentioned, Line 1 served as a control for Line 2 and Line 3 as no scaling inhibitor was added to the feed side of this line. The first microlayer (ca. 2 μm thick, Fig. 10) was an organic matrix with mineral inclusions of a roughly circular shape less transparent to the electron beam than the matrix. Individual particles that constituted the inclusions were in the size range 50–100 nm and were composed of Al, P, and Ca, with lesser amounts of Si and Fe. Some inclusions were found to be rich in Cr or Ti. A part of the first microlayer, which is closest to the membrane, is 0.6 μm thick (not shown) and has the same elemental composition and morphology as the rest of this microlayer. The second microlayer (ca. 2μm thick, not shown) was a very homogeneous organo-mineral (C, O, Al, P, Ca) matrix with rare inclusions of individual mineral particles of semicircular shape that were composed of either Ti or P and Na. The third and forth nanolayers (ca. 50 nm, not shown) were essen-

tially organic with some S detected and the forth layer had some Na and Cl detected in it.

Line 2. Figure 11 shows TEM images of the fouling layer on the surface of the Module 1 membrane from Line 2. Four microlayers could be discerned based on their differences in morphology and chemical properties. The first microlayer (ca. 1 μm thick) with a very fine granular structure was composed of organic compounds and S. The second microlayer (ca. 1 μm thick) was an organic matrix with individual mineral particles. These particles contained Al, Ca, Na, and Cl and could be estimated to be ca. 30–60 nm in size. The third microlayer (ca. 0.5–1 μm thick) differed from the second one only by its relatively low concentration of mineral fraction and by the presence of Ti in these inclusions. The forth microlayer (at least 1.5–2 μm thick) was a matrix composed mostly of C and S with increasing amounts

Line 1

50 nm	2 µm	2 µm	300 nm

C O S	C O S	C O	C O s	C O S	C O
Na Cl		Al P Ca Si Na Cl	Al P Ca Si	Al P Ca Fe Na Cl	Si

100 nm   100 nm

Line 2

C O S	C O s	C O	C O S	C O
Na Si		P Ca Al Na Cl		Si

1.5 µm   2.5 µm   1 µm   1 µm   100 nm

Line 3

?	C O s	C O	C O S	C O
	Si Ca Na Cl	Si Ca Al Cl		Si

1 µm   1 µm   2 µm   500 nm   400 nm

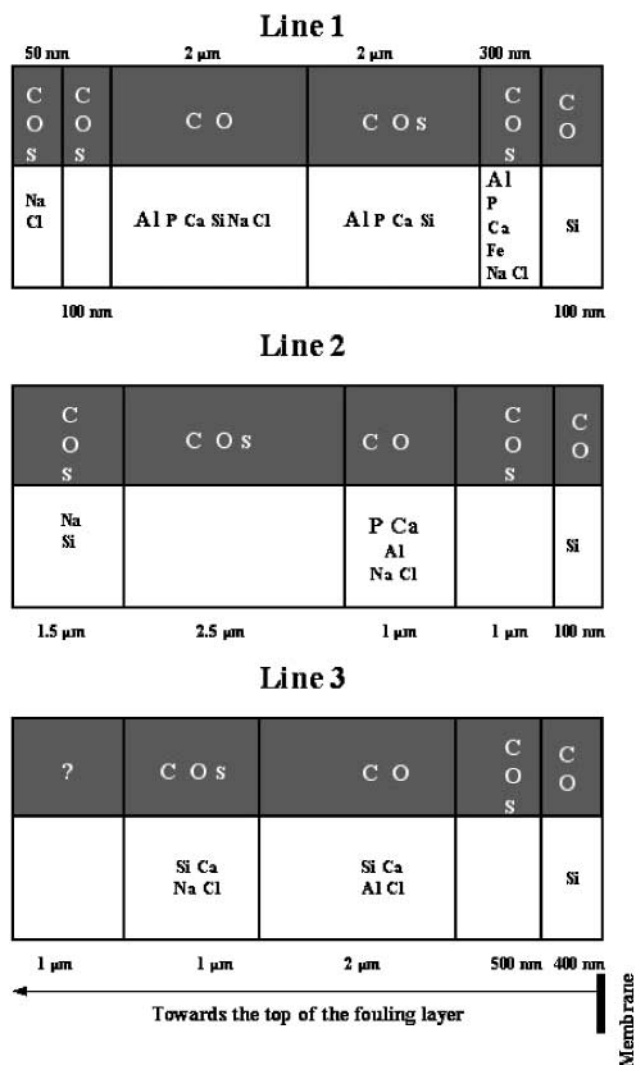← Towards the top of the fouling layer   Membrane

FIG. 13. Elemental composition of fouling layers for different doses of scaling inhibitor agent added.

of Si and Na. It had a concentration of mineral particles considerably lower than that of the third microlayer.

Line 3. As in the case of the membrane from Line 2, in Line 3 the first microlayer (0.3–0.5 μm thick, not shown) had a very fine homogeneously granular structure of the organic nature with particles no bigger than 1 nm dispersed over the layer. In the second microlayer (ca. 2 μm thick, Fig. 12) one observed chemically and morphologically essentially the same matrix as in the case of Line 1 containing fractal structure of mineral inclusions, which were finer than those observed in the Line 1 fouling layer (Fig. 10). The chemical composition of inclusions in Line 3 was also similar to that in Line 1 and Line 2 with the exception of phosphorus, which was present in Line 2 and absent in Line 3. The size of the individual mineral particles forming the fractal inclusion was in the 5–20 nm range. The third microlayer (ca. 1 μm thick, not shown) was an organo-mineral matrix composed of C, O, S, and Si and less abundant

in included mineral particulates (Cl, Na, and Ca) than the second microlayer.

Quantitative analysis of TEM images of fouling layers. TEM images of fouling layers formed in Line 2 and Line 3 were analyzed using the public domain NIH Image program, Version 1.62 (developed at the U.S. National Institutes of Health and available on the Internet at http://rsb.info.nih.gov/nihimage/). First, the original images were converted to 8-bit grayscale pictures (256 shadows of gray from 0 to 255). Second, a 2D rolling ball algorithm was used to remove the smooth continuous background from the images. The images were further converted to binary pictures by thresholding, that is, setting all pixels to either black (255) or white (0). Each binary image was subjected to a sequence of erosions followed by a sequence of dilations, the morphological operation known as "opening" which allows for the recovery of the most of the original features of the image while removing isolated pixels and producing a smoothed shape (28). A combination of the threshold value and the number of erosions/dilations was optimized to ensure that none of the essential details of the image was lost. Both binary images were then divided into several square subimages and fractal dimensions of mineral inclusions for each of the subimages were calculated. This was done using a box-counting algorithm (26) implemented in the public domain Java image processing program ImageJ, Version 1.24 (available at http://rsb.info.nih.gov/ij/). The size of the biggest "box" was chosen not to exceed the characteristic size of a subimage domain occupied by dendrites. In this fashion, four and two values with standard deviations corresponding to 95% confidence interval were obtained for dendritic structures in the fouling layers formed in Lines 3 and 2, respectively. A weighed average procedure, where individual measured values are weighed according to the magnitude of their standard deviations, was used to estimate true values for both cases. Values of fractal dimensions of 1.71 ± 0.04 and 1.55 ± 0.03 were calculated for dendritic structures in the fouling layers formed in Lines 2 and 3, respectively. The almost perfect scaling indicated that the mineral inclusions were indeed fractals.

DISCUSSION

Although both chemical heterogeneity and polydispersivity are attributes of most particle laden flows encountered in nature and engineering practice, previous efforts have addressed primarily the effects of polydispersivity and, generally, of the long-range transport of particles on the morphological properties of deposits (9, 29, 30). The focus of this work was on a less studied aspect—the relationship between the chemical composition of the suspension and the deposit morphology. The first step made in this direction was studying the effect of α and comparing it with that of N_{Pe}. It was found that differences in the surface chemistry of particles, on the one hand, and in particle size, on the other, have different effects on the morphology of deposits.

As can be seen from a comparison of Fig. 5 and Fig. 6, for deposits formed of very neutral (noncohesive, low α) particles,

the least accessible sites do not dominate the GSPD. This is in contrast to the case of deposits formed under very ballistic conditions (high N_{Pe}) characterized by the same fractal dimension. A decrease in α leads to the formation of a surface with a distribution of adsorption sites that is more homogeneous in terms of accessibility than that for a deposit with the same D but formed at higher N_{Pe}. This property may be employed for the development of analytical tools such as chemically and morphologically well-defined substrates employed as catalytic surfaces (31) or as substrates for the spectroscopic detection of traces of contaminants in aquatic solutions (32).

Simulations did not consider the role of breakup or rearrangement. For the case of chemically uniform suspensions, simulations are therefore more likely to be applicable to the top layer of a growing deposit before reorganization takes place. The dependence of D on α for the bulk of the deposit can be expected to be very different from that predicted for the top layer of the deposit (Fig. 4). In fact, fractal dimension may be expected to increase with an increase in α for the reason that the stickier particles are the closer the packing may be achieved after the breakup and compression of the deposit.

Deposition from Heterogeneous Suspensions: Comparison with Experiments

In the TEM images of fouling layers, patterns similar to those produced in the simulations were observed. An organic matrix of particles was found to surround dendritic structure of mineral particles (Figs. 10–12). The dendrites had different structures dependent on the amount of the scaling inhibitor added. We observe that mineral inclusions in Line 3 deposits are characterized by fractal dimensions lower than those in the fouling layers produced in Line 2. Dendritic structures appear to be virtually absent from the deposits in Line 1. Some insight into the origins of these structures is gained from an interpretation of the fouling layer formation in terms of a deposition process involving two types of particles (organic and mineral). We consider the case where organic particles ("gray") are more stable in water than are mineral particles ("black") $\alpha_{gg} \leq \alpha_{bb}$. This is anticipated based on the relatively higher charge density per mass for organic macromolecules of natural origin compared with mineral particles and on the potential for steric repulsion. Some interaction between mineral particles and organic fraction is expected to occur, however. These interactions are likely to take place in solution rather than during the deposition phase. As a result we would anticipate our "mineral" particles to include an adsorbed organic layer on the surface. Due to restrictions in molecular conformation, adsorption of organic matter will be (increasingly) limited once an initial layer has adsorbed. During the deposition process, this will result in much less interaction between organic "particles" and the mineral particles with previously adsorbed organic matter. Thus, $\alpha_{gb} \ll \alpha_{gg} < \alpha_{bb}$. Under these conditions for particle deposition, a range of deposit morphologies is predicted to occur that bear a striking resemblance to the images obtained from fouled membrane deposits.

In the absence of scaling inhibitor, it is possible that precipitation occurred near the surface of the membrane during the process of fouling layer growth. The addition of scaling inhibitor appears to result in the formation of small scaling inhibitor–metal nanoparticles approximately 50 nm in size. At low doses of scaling inhibitor, the morphology of the fouling layer observed in Line 2 is consistent with the deposition of these particles on the membrane surface along with organic matter. At higher doses of scaling inhibitor, the metals should be present nearly entirely as scaling inhibitor–metal nanoparticles, which deposit in a fashion similar to that observed in model simulations. The higher the dosage of the scaling inhibitor, the more clustering and the sharper the transition between the matrix and inclusions that may be expected in a fouling layer, as was indeed the case (Figs. 10–12).

This interpretation is corroborated by the results of quantitative analysis of the morphology of the fouling layers observed in our experiments (see *Quantitative analysis of TEM images of fouling layers* under Experimental Results). Values of fractal dimension of 1.71 ± 0.04 and 1.55 ± 0.03 were calculated for dendritic structures formed in Lines 2 and 3, respectively. The almost perfect scaling indicated that the mineral inclusions were indeed fractals. Lower fractal dimensions are typical for more open, sparse structures such as the dendritic pattern in the Line 3 fouling layer, when individual nanosized inhibitor–metal particles diffusively deposit on the membrane surface and form branching structures supported by the matrix material. Thus, the finer structure and the correspondingly lower fractal dimension of metallic inclusions observed in Line 3 in comparison with those in Line 2 correlate well with the fouling mechanism hypothesized in this work.

Implications for Membrane Filtration

Trends in deposit morphology predicted by the model for the deposition of heterogeneous suspensions are qualitatively similar to observations of fouling in a field study. Different degrees and patterns of segregation of particles from chemically distinct fractions of the suspension were predicted to occur in the fouling layer. The presence of more than one particle fraction leads to the formation of viable dendritic structures in the deposit. The dendrites formed from particles from the more cohesive fraction, otherwise fragile and subject to breakup, were predicted and observed to be surrounded and thereby supported by particles from the less cohesive fractions of the suspension. This finding has several important implications in the context of membrane fouling. In a chemically heterogeneous deposit, the propensity of the chemically distinct fractions to be eroded/resuspended and their response to backflushing (for porous filters) are expected to differ. More importantly, the model of resistances in series for a fouling layer's resistance to the permeate flow should be reconsidered. The deviation from the chemical homogeneity in the suspension to be filtered may result in the formation of fouling layers consisting of substructures of different specific resistances to permeate flow. In this situation, some pathways for the permeate flow through the fouling layer appear to be more

favorable than others. The more complex pathways composed of both resistances in series and in parallel are formed. As a result, when the suspension is chemically heterogeneous, the total resistance of the fouling layer is less than that predicted from a simple model of resistances in series. Chemical pretreatment may therefore be expected to significantly affect the resistance of fouling layers.

In the case of the crossflow filtration, the particle transport is expected to become more ballistic. When the no-slip condition does not hold at the fouling layer–suspension interface, crossflow takes on even more importance. Such a deposition regime is characterized by higher N_{Pe} values and is predicted to result in denser fouling layers with chemically distinct substructrues becoming more elongated in the direction normal to the membrane surface. The model of resistances in series becomes even less applicable under such conditions.

SUMMARY

In the present paper, the hypothesis that the morphology of fouling layers can be predicted based in part on the knowledge of transport and the surface chemistry of the particles that form the fouling layer was tested. We studied the relationship between the chemical composition of the suspension and the morphological properties of the deposit formed from the suspension. Results of the deposition modeling were qualitatively compared with TEM and EDX analysis of fouling layers produced in a series of pilot filtration experiments.

Differences in the deposit morphology induced by changes in the surface chemistry of particles were found to differ from those induced by changes in particle size. For the case of deposition from binary suspensions, different degrees of segregation of chemically distinct particulate fractions in the fouling layer were observed. The model predicted that particles from a cohesive fraction of the suspension form a network-like structure while noncohesive particles fill the spaces between this network and provide support for these structures. Particles from the noncohesive fraction were found to dominate the surface of generated deposits. Similar deposition patterns were observed in the pilot filtration experiments; the fouling layers consisted of an organic matrix with dendritic inclusions of a metallic nature incorporated in it. The fractal dimension of inclusions was found to be dependent on the suspension pretreatment protocol.

These findings prompt reevaluation of the model of resistances connected in series for the fouling layer resistance usually employed to describe permeate flow. Chemical heterogeneity of suspension may result in the formation of fouling layers with substructures of different specific resistances to permeate flow. The total resistance can be expected to be less than predicted in the assumption of a chemically homogeneous suspension.

ACKNOWLEDGMENTS

REFERENCES

1. Waite, T. D., Schafer, A. I., Fane, A. G., and Heuer, A., *J. Colloid Interface Sci.* **212**(2), 264–274 (1999), doi:10.1006/jcis.1998.6040.
2. Lin, C. L., and Miller, J. D., *Chem. Eng. J.* **80,** 221–231 (2000).
3. Belfort, G., Davis, R. H., and Zydney, A. L., *J. Membr. Sci.* **96,** 1–58 (1994).
4. Bowen, W. R., and Jenner, F., *Chem. Eng. Sci.* **50**(11), 1707–1736 (1995).
5. Wiesner, M. R., Clark, M. M., and Malleviale, J., *J. Environ. Eng.* **115**(1), 20–40 (1989).
6. Romero, C. A., and Davis, R. H., *Chem. Eng. Sci.* **45**(1), 13–25 (1990).
7. Sethi, S., and Wiesner, M. R., *J. Membr. Sci.* **136,** 191–205 (1997).
8. Huisman, I. H., and Trägårdh, C., *Chem. Eng. Sci.* **54,** 271–280 (1999).
9. Yoon, S.-H., Lee, C.-H., Kim, K.-J., and Fane, A. G., *J. Membr. Sci.* **161,** 7–20 (1999).
10. Tarabara, V. V., Hovinga, R. M., and Wiesner, M. R., *Environ. Eng. Sci.* **19**(5), 272–281.
11. Wiesner, M. R., and Chellam, S., *Environ. Sci. Technol.* **33**(17), 360A–366A (1999).
12. Wiesner, M. R., *J. Environ. Eng.* **125**(12), 1124–1132 (1999).
13. Huisman, I. H., Elzo, D., Middelink, E., and Trägårdh, C., *Colloid. Surf. A* **138,** 265–281 (1998).
14. Lee, Y., and Clark, M. M., *J. Membr. Sci.* **149,** 181–202 (1998).
15. Chellam, S., and Wiesner, M. R., *J. Membr. Sci.* **138,** 83–97 (1998).
16. Faibish, R. S., Elimelech, M., and Cohen, Y., *J. Colloid Interface Sci.* **204**(1), 77–86 (1998), doi:10.1006/jcis.1998.5563.
17. Hwang, K.-J., Liu, H.-C., and Lu, W.-M., *J. Membr. Sci.* **138,** 181–192 (1998).
18. O'Melia, C. R., and Stumm, W., *AWWA J.* **59**(11), 1393–1412 (1967).
19. Kim, H., and Rajagopalan, R., *Chem. Eng. Commun.* **108,** 147–164 (1991).
20. Elimelech, M., Gregory, J., Jia, X., and Williams, R. A., "Particle Deposition and Aggregation." Butterworth–Heineman, Stoneham, MA/London, 1995.
21. Veerapaneni, S., and Wiesner, M. R., *J. Colloid Interface Sci.* **162**(1), 110–122 (1994), doi:10.1006/jcis.1994.1015.
22. OMelia, C. R., and Tiller, C. L., *in* "Environmental Particles" (J. Buffle and H. P. van Leeuwen, Eds.), Vol. 2, p. 353. Lewis Publishers, London, 1992.
23. Ventresque, C., Gisclon, V., and Bablon, G., and Chagneau, G., *Desalination* **131**(1–3), 1–16 (2000).
24. Tarabara, V. V., and Wiesner, M. R., *J. Colloid Interface Sci.* **237**(1), 150–151 (2001), doi:10.1006/jcis.2001.7479.
25. Mandelbrot, B. B., "The Fractal Geometry of Nature." Freeman, New York, 1983.
26. Vicsek, T., "Fractal Growth Phenomena." World Scientific, Singapore, 1992.
27. Parron, C., and Pierrisnard, F., "Autopsie des membranes colmatés de la première tranche d'essais (Juin-Septembre 1999)," Université Aix-Marseille III-CNRS, Centre Européen de Recherche et d'Enseignement de Géosciences de l'Environnement, 2000.
28. Russ, J. C., "Computer-Assisted Microscopy: The Measurement and Analysis of Images." Plenum, New York, 1990.
29. Meakin, P., Ramanlal, P., Sander, L. M., and Ball, R. C., *Phys. Rev. A* **34**(6), 5091–5103 (1986).
30. Veerapaneni, S., and Wiesner, M., *Environ. Sci Technol.* **31,** 2738–2744 (1997).
31. Lee, C.-K., and Lee, S.-L., *Heterog. Chem. Rev.* **3,** 269–302 (1996).
32. Vodinh, T., *Trends Anal. Chem.* **17**(8–9), 557–582 (1998).